Materials Today Bio 31 (2025) 101516

Contents lists available at ScienceDirect

Materials Today Bio

journal homepage: www.journals.elsevier.com/materials-today-bio

Enhancing auricular reconstruction: A biomimetic scaffold with 3D-printed multiscale porous structure utilizing chondrogenic activity ink

Yueying Kong [a,1], Zijing Lu [c,1], Jianan Zhan [e], Xi Zhou [d], Shenghua Chen [a], Qiwei Chen [d], Haihuan Gong [f], Xianlin Zhang [d], Xiaoyan Mao [c,*], Yilin Wang [b,**], Wenhua Huang [a,d,e,***]

[a] *Clinical Anatomy & Reproductive Medicine Application Institute, Hengyang Medical School, University of South China, 421001, Hengyang, China*
[b] *Department of Human Anatomy, College of Basic Medical Science, China Medical University, 110122, Shenyang, China*
[c] *Department of Plastic and Aesthetic Surgery, Nanfan Hospital of Southern Medical University, No. 1838 N Guangzhou Rd, 510515, Guanzhou, China*
[d] *Guangdong Provincial Key Laboratory of Medical Biomechanics, National Key Discipline of Human Anatomy, School of Basic Medical Sciences, Southern Medical University, 510515, Guangzhou, China*
[e] *Department of Human Anatomy, School of Basic Medical Sciences Guangdong Medical University, 524000, Zhanjiang, China*
[f] *Department of Periodontics, Guangzhou Key Laboratory of Basic and Applied Research of Oral Regenerative Medicine Affiliated Stomatology Hospital of Guangzhou Medical University, Guangzhou, 510182, China*

ARTICLE INFO

Keywords:
Auricle deformity
Cartilage reconstruction
Auricle reconstruction
Tissue engineering
3D printing

ABSTRACT

Auricular defects are highly prevalent and have a significant impact on the physical and mental well-being of patients. However, due to the intricate anatomy of the auricle, achieving personalized and precise reconstruction poses a major challenge. Currently, tissue engineering auricle scaffolds based on rigid materials are an effective therapeutic approach for auricle reconstruction. Nevertheless, these auricular scaffolds often fail to meet biomechanical requirements and lack biological activity, resulting in suboptimal treatment outcomes. In this study, polyvinyl alcohol and gelatin were used as printing inks, and nano-silica was employed as a filler to optimize the printability of the inks. Through layer-by-layer 3D printing, auricle scaffolds were fabricated that closely mimic human auricular biomechanical properties and possess a multi-scale pore structure. Subsequent in vitro experiments confirmed the biocompatibility of the scaffolds. Furthermore, a rabbit auricular cartilage defect model was established to evaluate the therapeutic efficacy of this bionic scaffold featuring a multi-scale pore structure for auricle defects. The findings demonstrated that the developed auricle scaffold not only exhibited excellent biomechanical strength and favorable biocompatibility but also provided an advantageous environment for chondrocyte growth due to its multi-scale pore structure, thereby significantly promoting chondrocyte proliferation. Overall, the 3D printed tissue engineering bionic scaffold with a multi-scale pore structure developed in this study is anticipated to significantly enhance the therapeutic efficacy for auricle defects and offer a novel therapeutic strategy for such defects.

1. Introduction

Auricular defects and deformities encompass both congenital auricular deformities as well as acquired defects resulting from trauma, burns, tumors, puncture defects, and scars [1]. The prevalence of auricular defects is approximately 5.18 cases per 10,000 individuals [2]. Such deformities not only affect facial aesthetics but also contribute to varying degrees of hearing impairment, thereby impacting both the physical and mental well-being of individuals [3]. Due to the complex anatomy and delicate physiology of the auricle, reconstructive procedures remain a significant challenge in clinical practice [4]. Compared to traditional autologous costal cartilage transplantation, tissue engineering offers substantial advantages by reducing surgical complexity, shortening operation time, and minimizing postoperative complications [5–7]. At present, the most commonly used materials for preparing tissue engineering auricular supports are high-density polyvinyl alcohol

---

* Corresponding author.
** Corresponding author.
*** Corresponding author.
E-mail addresses: drmaoxy@163.com (X. Mao), 20242252@cmu.edu.cn (Y. Wang).
[1] These authors contributed equally to this work.

https://doi.org/10.1016/j.mtbio.2025.101516
Received 26 October 2024; Received in revised form 18 January 2025; Accepted 20 January 2025

(HDPE) [8], Poly-caprolactone (PCL) [9] and polyurethane [10,11] with high mechanical strength. However, these materials have limitations in terms of plasticity, mechanical properties, and cell adhesion, often resulting in leakage, rupture, and infection after implantation [8,12]. Additionally, the majority of these materials possessing high mechanical strength only marginally replicate the fundamental morphology of the auricle based on its appearance, lacking biological functionalities that hinder effective auricular cartilage repair. Therefore, the development of tissue engineering auricular scaffolds that conform to the biomechanical characteristics of human auricular cartilage as well as possess biological functionalities has emerged as a pressing issue in the field of auricular defect treatment [13].

The development of hydrogels, such as hyaluronic acid [14], GelMA [15,16] and alginate [17], provides a promising strategy for the preparation of ideal auricular scaffolds. Hydrogels exhibit excellent biocompatibility and biodegradability, along with a loose, porous microstructure that promotes cell adhesion and tissue growth [18]. Among these, polyvinyl alcohol (PVA) is a highly safe polymeric organic compound widely used in biomedical applications because of its high water content and elasticity in soft tissues [19]. Owing to the absence of cell-adhesive properties and the inherently high hydrophilicity of PVA on its surface, it is challenging for cultured cells to adhere and thrive on PVA substrate [20]. It has been documented that gelatin (Gel), a collagen-derived biopolymer, exhibits excellent biocompatibility and biomimetic properties [21]. The incorporation of Gel into alginate enhances biocompatibility, facilitates cell adhesion and proliferation, and augments the mechanical properties and strength of the resulting composite [22]. However, due to the intricate and variable morphology of the human auricle, accurately molding this kind of three-dimensional structure using flexible PVA-Gel hydrogels remains a significant challenge. Therefore, it is crucial to determine a molding process that can achieve excellent accuracy while guaranteeing the integrity of the scaffolds after implantation.

3D printing is a rapid fabrication technique that enables the creation of 3D structures resembling functional tissues and organs with intricate architectures [23,24]. In the commonly used 3D printing process, direct ink writing (DIW) stands out as a more prevalent manufacturing technology due to its diverse material options, high printing speed, and high printing accuracy [25]. These features make DIW particularly suitable for the fabrication of tissue engineered auricular cartilage [26]. DIW works by loading bioink into a syringe barrel and extruding through the tip of a micronozzle for rapid preparation of various complex structures [27]. However, the effectiveness of DIW is constrained by the rheological properties of the printing ink [28]. Gravity presents a significant challenge in high resolution and fidelity when printing intricate 3D structures in air using low-viscosity fluid materials [29]. Consequently, appropriately increasing the viscosity of bioink can enhance both printability and fidelity. Several studies have opted to incorporate nanomaterials, such as nanofibers [30,31], nano-silicate [32], and nanohydroxyapatite [33]. Among them, nanometer silicon dioxide (SiO_2) particles with a larger specific surface area can establish a tighter interface with the polymer matrix, thereby improving the stiffness and shear modulus of the ink while also adjusting its mechanical properties [34]. In addition, SiO_2 has significant potential for cartilage regeneration [35].

Based on these views, in this study, we aimed to develop a printing ink with cartilage activity to fabricate a tissue engineering bionic auricular scaffold that closely mimics the biomechanical properties of human auricular cartilage and possesses a multi-scale pore structure. Specifically, Gel was used to modulate the cell adhesion and mechanical properties of PVA. The incorporation of nano-silica enhanced the printability and augmented the chondrogenic performance of the ink. The biocompatibility of the printing ink was evaluated through both in vivo and in vitro experiments. Finally, the rabbit auricular cartilage defect model was established to validate the efficacy of the bionic scaffold with multi-scale porous structure for treating auricle deformities. This model enabled us to assess how well the scaffold promoted auricular cartilage repair. The results confirmed the adaptability of the biomimetic scaffold to auricular cartilage defects, its ability to repair the structural defect, and its potential in promoting the growth of surrounding auricular chondrocytes (Fig. 1).

2. Experimental

2.1. Preparation and cross-linking of printing inks

The 100 mg mL^{-1} solution of PVA (MW = 205,000 g mol^{-1}, Aladdin, China) was prepared by dissolving PVA powder in deionized water at 90 °C under magnetic stirring for 8–10 h. The magnetic stirring speed was maintained at 200–250 rpm min^{-1} to avoid the foaming of PVA. According to the mass ratio of Gel: PVA solution = 1:10 weighed appropriate amount of PVA solution and gelatin particles (G1890, Sigma Aldrich). The P/G solution was prepared by dispersing gelatin particles in PVA solution and magnetically stirring the mixture at 60 °C for 2–3 h at a rate of 150–200 rpm min^{-1} until fully dissolved. According to the mass ratio of SiO_2: P/G solution = 5:100 was weighed appropriate amount of P/G solution and nanometer silica (Aladdin, China). Similarly, the P/G/Si solution was prepared by dispersing nanometer silica in P/G solution and magnetically stirring the mixture at 60 °C for 2–3 h at a rate of 150–200 rpm min^{-1} until fully dissolved. Subsequently, the PVA, P/G, and P/G/Si solutions were poured into 60 mm Petri dishes and dried at 37 °C to obtain thin-film uncrosslinked scaffolds. The uncrosslinked scaffolds were immersed in 6 mol L^{-1} sodium hydroxide for 8–12 h to obtain three types of cross-linked scaffolds. These scaffolds were then washed through repeated immersion in deionized water until a pH of 7 was attained, prior to further experimentation.

2.2. Characterization of printing inks

Chemical characterization. The PVA, P/G, and P/G/Si printing inks were characterized using FTIR (Fourier-transform infrared, Thermo Nicolet iS5, USA) with 400–4000 cm^{-1} recording range. ^1H NMR analyses were performed on the spectrometer (^1H nuclear magnetic resonance, BRUKER AVANCE-III 500 MHZ) at room temperature.

Scanning electron microscopy (SEM) analysis. SEM (Sigma 500, Germany) was utilized to analyze the microstructure of the PVA, P/G, and P/G/Si printing inks. First, all the printing inks were subjected to freeze-drying treatment to reveal their internal structure. Subsequently, the printing inks were placed on a copper stud and coated with gold/palladium sputtering before analysis.

Water contact angle. The surface hydrophilicity of PVA, P/G, and P/G/Si printing inks were evaluated by measuring the static aqueous contact angles using a contact angle measurement (SL250, USA) instrument. Briefly, the freeze-dried printing inks were placed flat on a clean glass slide and then transferred to a horizontal detection table. Each drop of 2 μL of deionized water was dropped on the surface of the hydrogels at room temperature and images were taken with a camera.

Swelling behavior. To evaluate the swelling behavior of the scaffolds, each PVA, P/G, and P/G/Si printing inks were measured after freeze-drying (W_d). Next, the printing inks were placed in PBS buffer and incubated in an incubator at 37 °C for 24 h to swell, and then the surface PBS was removed with filter paper and weighed (W_s). The swelling ratio of the hydrogel was calculated as follows: $SR= (W_s - W_d)/W_d \times 100\ \%$.

Degradation behavior. To evaluate the in vitro degradation properties of the scaffolds, each PVA, P/G, and P/G/Si printing inks was measured after freeze-drying. The hydrogels were immersed in PBS and incubated at 37 °C for 28 days at a constant oscillation of 100 rpm min^{-1}. PBS was replaced every 3–4 days. The hydrogels of the group were taken out at 7,14,21 and 28 days, respectively. The samples were rinsed with distilled water, dried in an oven at 37 °C for 48 h and weighed.

Rheology and printability analysis. The storage modulus (G') and loss modulus (G'') of PVA, P/G, and P/G/Si printing inks were obtained by

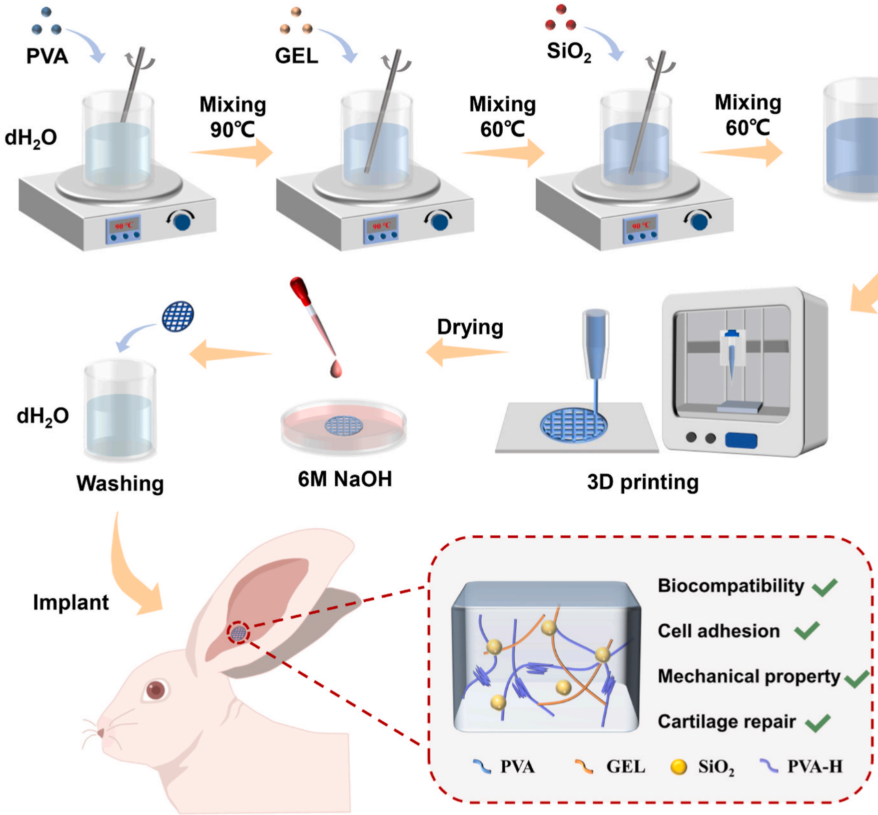

Fig. 1. Schematic diagram of the process of 3D-P/G/Si scaffold preparation and implantation.

rheometer (HAAKE MARS 40, Germany), subjecting them to shear strain from 0.1 % to 100 % at a constant frequency of 1 Hz. Flow and viscosity curves for printing ink were obtained through rotational tests featuring shear rate scanning ranging from 0.1–100 s^{-1}. Additionally, the temperature dependence of printing inks were analyzed by setting the temperature range of 10–40 °C and the heating rate of 5 °C/min.

2.3. *Preparation and characterization of 3D-P/G/Si scaffolds*

The 3D-P/G/Si scaffold was designed by Solidworks software and then printed using a 3D bioprinter (Envision, Germany). Printed the configured P/G/Si printing ink into a multi-layer bracket with a predesigned square shape (10 × 10 × 2 mm) or a circular shape (10 mm in diameter and 2 mm in height). That 3D printed scaffold was immersed in 6 M NaOH for crosslinking, and then washed with deionized water to PH = 7 for subsequent experiments. Subsequently, the ink parameters of the substrate layer were analyzed using printing nozzles with gauges of 18 G, 20 G, and 22 G to investigate the correlation between printing parameters and filament diameter. The printing temperature was set at 15 °C, while the printing pressure ranged from 1.5–2.5 bar. For an 18 G print nozzle, the ink extrusion speed was adjusted between 2–6.5 mm s^{-1}. When utilizing a 20 G print nozzle, the ink extrusion speed ranged from 2–7 mm s^{-1}. Similarly, for a 22 G print nozzle, the ink extrusion speed varied from 2–8.5 mm s^{-1}. All scaffolds were observed under a microscope (BX53 Olympus Japan) to screen them and determine optimal printing parameters rapidly. According to the optimal printing parameters, a multi-layer 3D-P/G/Si scaffold with a pore of 400 μm was prepared by printing with a 22 G nozzle. The 3D-printed scaffolds were freeze-dried and coated with a gold/palladium sputter. Their microstructure was subsequently analyzed using SEM.

2.4. *Mechanical properties of 3D-P/G/Si scaffolds*

Next, we conducted tensile property tests on a biaxial tensile testing machine (LS1, Ametek, USA). Initially, PVA, P/G, and P/G/Si scaffolds ($n = 3$) were precisely cut into dimensions of 100 × 30 × 1 mm (length × width × height). Subsequently, the two ends of each specimen were securely fastened to the testing machine for conducting tensile tests at room temperature with a speed of 10 mm min^{-1} until fracture occurred. The recorded test data were meticulously analyzed to determine the Young's modulus of the three scaffolds. Additionally, dumbbell-shaped 3D printed specimens featuring interlacing structures in both transverse and longitudinal directions were employed for further tensile testing. The dumbbell-shaped specimens ($n = 3$) with pore sizes of 0, 400, and 800 μm were securely affixed to the testing machine at both ends. The test and calculation methods employed were consistent with those previously described.

2.5. *Biocompatibility in vitro*

The biocompatibility of four scaffolds ($n = 12$), including PVA group, P/G group, P/G/Si group and 3D-P/G/Si group, was evaluated using human chondrocytes (C28/I2 cells). The C28/I2 cells were cultured in a complete medium at 37 °C and 5 % CO_2. The medium was refreshed every 2–3 days until a cell confluence of 90 % was achieved before commencing the experiment. All scaffolds underwent sterilization with 75 % ethanol for 1 h, followed by removal of residual ethanol through DPBS washing and subsequent sterilization under UV light irradiation for 2 h. The C28/I2 cells were seeded onto various scaffold groups at a density of 0.5×10^4 cells/well in a 48-well culture plate and incubated. The proliferation of C28/I2 cells was evaluated by Alamar Blue reagent (Invitrogen, USA) on days 1, 3, and 5 post-culture. Prior to usage, the Alamar Blue reagent was diluted at a ratio of 1:10 with a complete medium. Subsequently, 300 μL of the diluted reagent was added to each well. Following an incubation period of 4 h at 37 °C in an incubator, 100 μL of the solution from each well was transferred to a 96-well plate for analysis. The results were then measured using a multifunctional fluorescent microplate reader (BioTek/SYNERGY, USA) at a wavelength of 530/560 nm. Additionally, the viability of C28/I2 cells was also evaluated on days 1, 3, and 5. Upon examination under a fluorescence microscope (IX 83, Olympus, Japan), live cells exhibited green staining while dead cells displayed red staining.

2.6. *Toxicity in vivo*

Animal experiments were performed following the guidelines for the care and use of laboratory animals established by the Animal Laboratory of Nanfang Hospital and had been approved by the Ethical Committee for Laboratory Animals. The approval date was March 2023, and the approval number was IACUC-LAC-20230317-010. Sprague-Dawley (SD) rats aged 6 weeks, weighing an average of 160–180 g, were utilized in the experiment. The SD rats were randomly divided into five groups ($n = 3$): PVA group, P/G group, P/G/Si group, 3D-P/G/Si group, and control group. HDPE is a medical polymer known for its excellent biocompatibility, non-degradability, and non-toxicity [36]. Currently, it is widely utilized in the field of ear reconstruction. Consequently, HDPE was selected as the control group for the in vivo experiments. The scaffolds were sterilized according to the previously described method. Before implantation, SD rats were anesthetized via intraperitoneal injection of Pentobarbital Sodium (45 mg kg^{-1}). The scaffold was implanted between the skin and fascia on the rat's back. On days 14 and 28 after implantation, skin biopsies, including the scaffolds, and main organ were harvested for histological analysis. Tissues were fixed, dehydrated, embedded in paraffin, sectioned, and stained with hematoxylin and eosin (H&E) to evaluate their histocompatibility.

2.7. *The immunofluorescence staining of type II collagen*

The PVA, P/G, and P/G/Si scaffolds were sterilized according to the previously described method. Subsequently, the scaffolds were immersed in a cartilage induction medium and incubated at 37 °C for 24 h, resulting in the preparation of three types of leaching solutions. C28/I2 cells were cultured in these leaching solutions for 5 days, with the solutions being changed every 2–3 days. The cell slides were fixed with 4 % PFA (Macklin, China) and permeabilized using 0.2 % Triton X-100 (Macklin, China). Following blocking using the normal serum, the slides were incubated with anti-Collagen II (SAB, USA) overnight at 4 °C, and further incubated with a secondary antibody (Thermo Fisher, USA) for 1 h. The nuclei were stained with DAPI for 1 min. An inverted laser confocal microscope was used to stimulate and photograph at 488 and 594 nm.

2.8. *Application of auricular scaffolds in repairing rabbit auricular cartilage defects*

New Zealand white purpose-bred research rabbits (12 weeks old, weighing 2000 ± 300 g) were used to construct auricular cartilage defect models [37]. All the rabbits were randomly divided into five groups: PVA group, P/G group, P/G/Si group, 3D-P/G/S group, and control group. HDPE scaffolds were employed in the control group. The scaffolds were sterilized according to the previously described method. After administering anesthesia, an incision was made on the medial aspect of the rabbit auricular proximal to expose the auricular cartilage. A 10 mm diameter defect was created in the rabbit auricular cartilage using a sterilized round punch, ensuring that the dorsal skin of the rabbit auricular remained intact. The scaffolds were implanted into the defect areas and closed densely using absorbable sutures (4–0 nylon). After operation, all the rabbits were allowed free-cage activity. Following 1 and 3 months of scaffold implantation, rabbits were euthanized using a lethal dose of pentobarbital sodium, and their auricular cartilage was collected for subsequent evaluation. The repaired cartilages were fixed in 4 % para formaldehyde for two days. The repaired cartilages were then embedded in paraffin and sliced, and characterized by H&E (Sinoreagent, China), Alcian Blue (Sinoreagent, China), Masson (Solarbio, China), Safranin O and Fast Green staining (SO/FG) (Solarbio, China), and immunohistochemical staining for Collagen I, Collagen II (Sinoreagent, China).

2.9. *Statistical analysis*

Each group included at least three samples ($n \geq 3$), and all data were presented as Means ± Standard deviations. Because the values were normally distributed, the experimental data from all the studies were analyzed using a one-way analysis. When statistical differences appeared, the LSD test and Dunnett T3 test were performed for the post hoc multiple comparisons. Statistical significance was set at 5 % ($\alpha = 0.05$).

3. Results

3.1. *Preparation and cross-linking of printing inks*

As shown in Fig. 2Ai, we gained with a 10 % PVA solution. The PVA solution exhibited complete transparency and excellent fluidity. After the addition of Gel in proportion, the printing ink transformed into a translucent light yellow, while its fluidity remained relatively unchanged (Fig. 2Aii). When mixed with silica, the color of the solution changed significantly from light yellow to opaque milky white, while the fluidity was greatly reduced (Fig. 2Aiii). Subsequently, the compositional structure was analyzed by FTIR. The results indicated that PVA displayed the characteristic peak of the -OH group at 3000–3500 cm^{-1} [38], while the peak near 2900 cm^{-1} was attributed to the C-H bond of the alkyl group [39]. With the addition of Gel, the absorption peak shape of -OH gradually widened, and the peak at 917 cm^{-1} was the bending vibration of the C-H bond on the aldehyde group of Gel [40]. After the addition of silica, the strong and broad absorption bands at 832 cm^{-1} and 471 cm^{-1} were the symmetrical tensile vibration peaks of Si-O [41]. The ATR-IR results were in line with expectations, indicating the successful mixing and acquisition of the desired printing ink (Fig. 2B).

Subsequently, the three inks were individually poured into a Petri dish and dried to obtain thin films. Following cross-linking through immersion in 6 M NaOH and subsequent washing with deionized water, each film could be effortlessly detached from the Petri dish, confirming the successful completion of cross-linking. As shown in Fig. 2C, after the process of cross-linking, PVA retained its colorless and transparent appearance, whereas P/G/Si still exhibited an opaque milky white hue. Both colors remained similar to their respective states prior to cross-linking. However, the transparency of the cross-linked P/G was significantly diminished and its color transformed to white. This change can be attributed to the impact of environmental pH on the protein's electrical properties. The closer the pH approaches alkaline, the diminished repulsion between molecules results in aggregation, causing the previously miscible system to transition from transparency to opaqueness [38]. To further verify whether the cross-linking was successful, we conducted ^1H NMR spectroscopy on the materials before and after cross-linking with the third set of P/G/Si (Fig. 2D). Comparison with uncrosslinked hydrogel revealed a clear disappearance of H_a at 1.90–2.00 ppm in the ^1H NMR spectrum of crosslinked hydrogel, confirming our conjecture regarding cross-linking [42]. In summary, both ^1H NMR and ATR-IR results confirmed that expected product structures have been successfully synthesized using three printing inks capable of being cross-linked by 6 M NaOH.

3.2. *Characterization of printing inks*

The hydrophilicity of three printing inks was investigated through

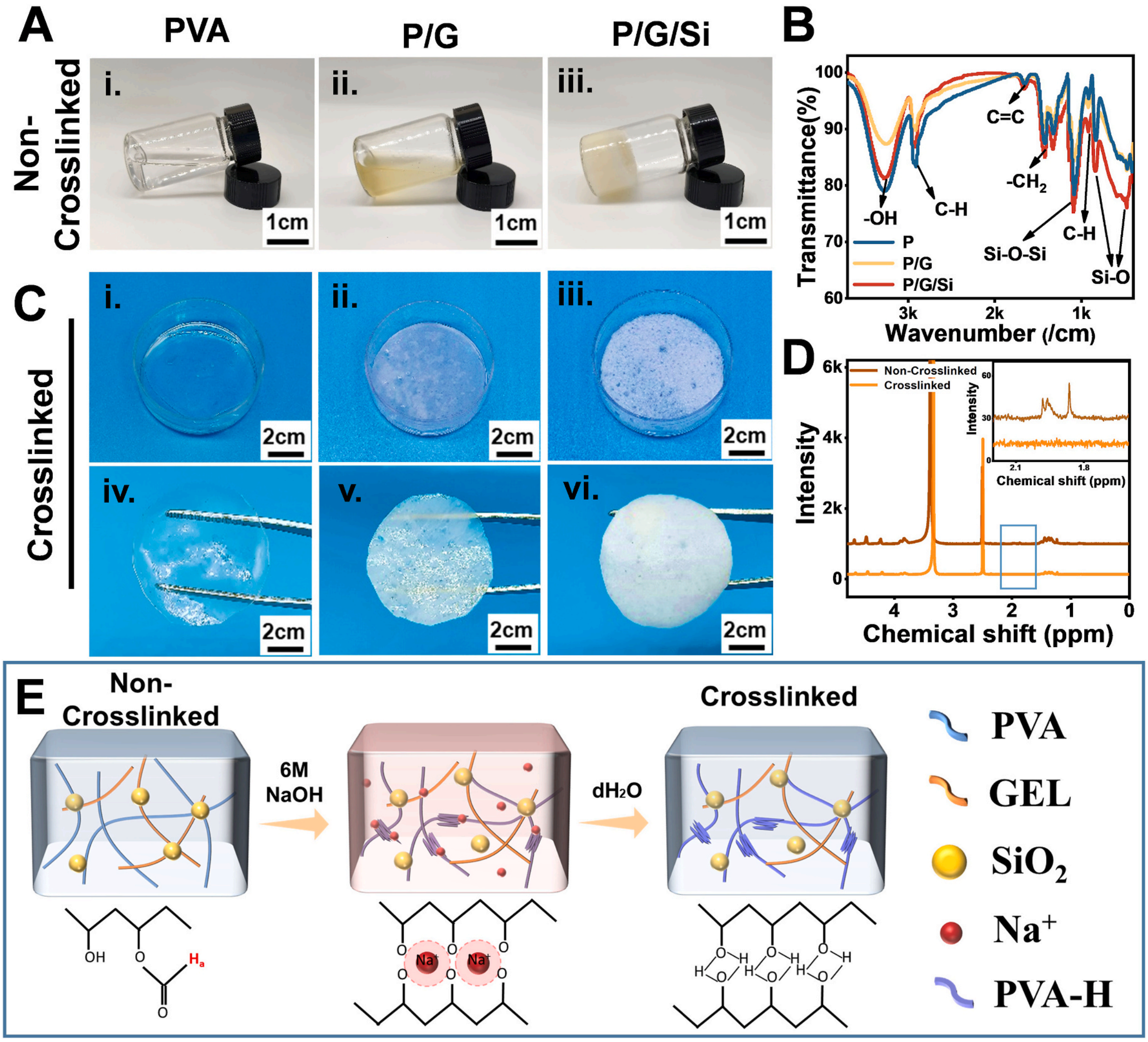

Fig. 2. Preparation and cross-linking of printing inks. (A) Comparison of fluidity and transparency of PVA, P/G, and P/G/Si printing inks before crosslinking. (B) FTIR spectra of PVA, P/G, and P/G/Si printing inks. (C) Comparison of transparency of PVA, P/G, and P/G/Si printing inks after crosslinking. (D) The ^{1}H NMR spectrum of uncrosslinked and crosslinked printing ink. (E) The schematic diagram of the mechanism of crosslinking with NaOH.(PVA-H: crosslinked PVA hydrogel).

static water contact angle analysis. Upon initial contact with water droplets, the surface of PVA exhibited a water contact angle of (50.90 ± 2.93) °, while P/G displayed a significantly larger angle of (57.10 ± 0.89) ° compared to PVA (Fig. 3Ai, ii). SEM characterization revealed that the PVA surface had a rough texture and small gaps, which were filled by gelatin particles upon its addition to the mixture, resulting in a smoother material surface that hindered water attachment (Fig. 3B i-iv). This could explain why P/G exhibited a higher water contact angle than PVA did. However, the first-second water contact angle for the P/G/Si group was only (42.76 ± 4.43) ° due to the presence of nano-silica particles with uneven sizes on the porous surface of P/G/Si as observed by SEM analysis (Fig. 3A iii, Fig. 3B v, vi). To facilitate a more comprehensive comparison of hydrophilicity among the three printing inks, we conducted further analysis on the dynamic water contact angle within the time range of 1–5 s. As the contact time increased, all hydrogels exhibited a decrease in water contact angle, with P/G/Si demonstrating a smaller angle compared to both PVA and P/G (Fig. 3A). Notably, at the fifth-second mark, the water contact angle of P/G/Si hydrogel was found to be less than 20°, indicating its exceptional ability for rapid water penetration and thus making it highly advantageous for cell adhesion. (Fig. 3A ix, Fig. S1, Supporting Information).

Then we conducted a swelling test. After 24 h of swelling, the swelling rate of PVA was recorded as (103.27 ± 11.45) %, while the swelling rate of P/G reached (133.74 ± 23.22) %, both surpassing that of the PVA group. Notably, the swelling rate of P/G/Si was measured at an impressive (326.61 ± 41.82) %, approximately three times higher than that observed in pure PVA scaffolds alone. Overall, it can be concluded that P/G/Si exhibited superior hydrophilicity, thereby facilitating cell adhesion and rendering it suitable for promoting cell proliferation (Fig. 3C–D, Fig. S2, Supporting Information). To confirm that the scaffold can remain stable for a long time after implantation in vivo, we also performed degradation. The three scaffolds ($n = 3$) were immersed in PBS for 7, 14, 21, and 28 days, respectively. As the degradation time increased, there was no significant change observed in the weight of all scaffold groups, indicating the excellent stability of the printing inks (Fig. 3E).

According to rheological analysis, the amplitude scanning results revealed that the G′ of P/G/Si printing ink surpassed the G″ within the shear strain range of 0.1 %–10 %, indicating its viscoelastic solid characteristics (Fig. 3F). In contrast, PVA printing ink only exceeded G″ in the lower shear strain range of 0.1 %–1 %, while P/G printing ink exhibited G″ greater than G′ at all shear strains, making it challenging to print. Considering the Gel's thermal sensitivity, further investigation was conducted on the temperature's impact on rheological properties of the printing ink [43]. Under a constant shear rate ($\gamma = 0.1\ s^{-1}$) and gradual heating from 10 °C to 40 °C, P/G/Si printing ink consistently maintained

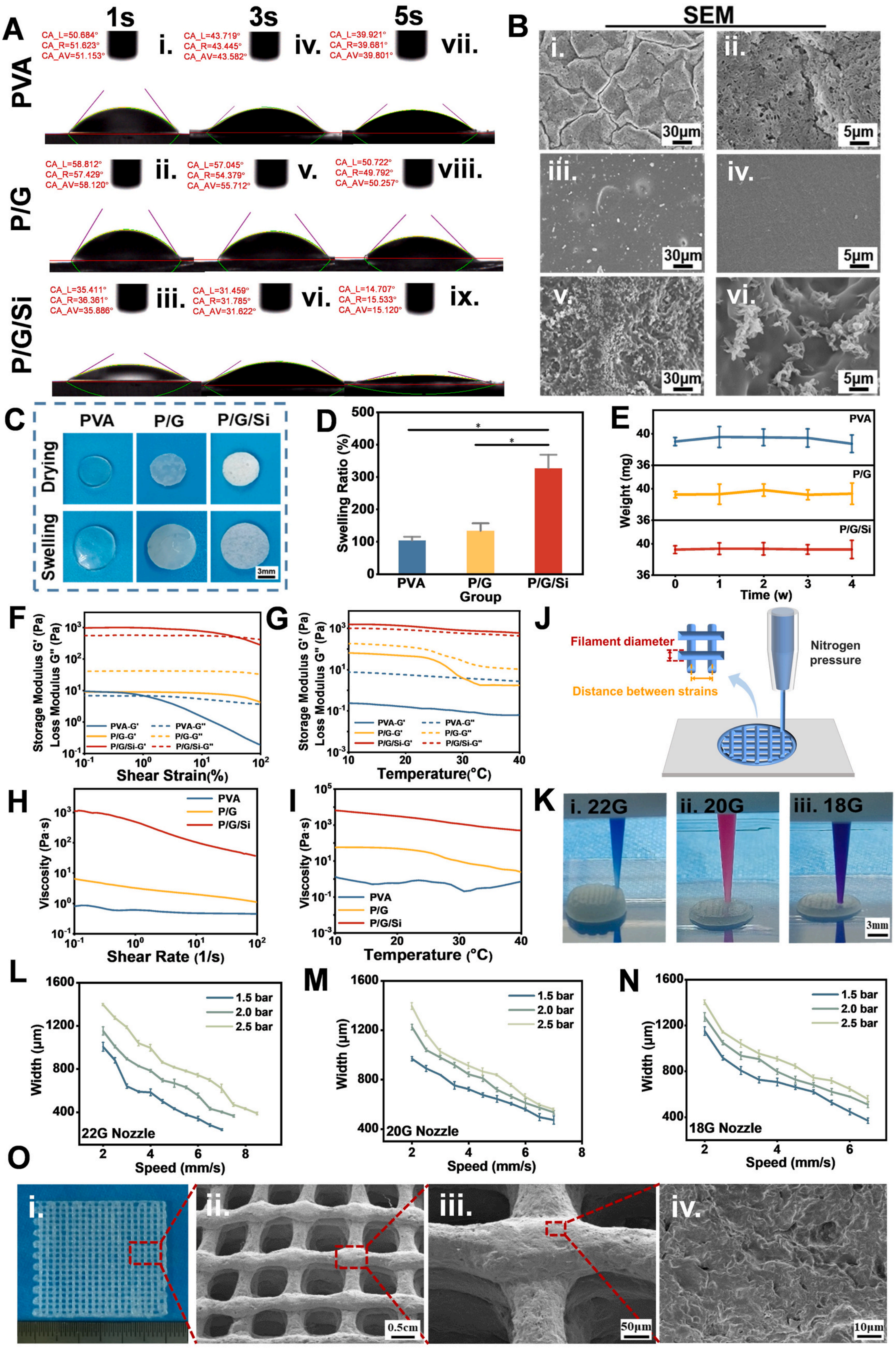

Fig. 3. Characterization of printing inks and 3D-P/G/Si. (A) The water contact angle of PVA, P/G, and P/G/Si printing inks. (B) SEM images of PVA, P/G, and P/G/Si printing inks. (C) Comparison of three printing inks before and after swelling. (D) Swelling ratio of PVA, P/G, and P/G/Si printing inks (n = 3). (E) Degradation test of PVA, P/G, and P/G/Si printing inks (n = 3). (F–I) Rheological properties of PVA, P/G, and P/G/Si printing inks. (J) Schematic illustration of the preparation of different filament diameters of 3D-P/G/Si scaffolds. (K) 3D printing under 22 G, 20 G and 18 G nozzle. (L–N) Optimum parameters for printing with 22 G, 20 G and 18 G nozzle (n = 3). (O) SEM images of 3D-P/G/Si scaffolds.

a higher G′ than G″, preserving its gel-like state as a viscoelastic solid (Fig. 3G). Additionally, to facilitate the extrusion of the printed ink through a small-diameter nozzle, the ink must exhibit shear thinning characteristics, wherein the apparent viscosity decreases with increasing shear stress or shear rate [44]. As depicted in Fig. 3H, at a temperature of 25 °C, all three groups of printing inks demonstrated a decreasing trend in viscosity as the shear rate decreased. There, P/G/Si exhibited the most significant decrease. Even when subjected to temperature variations (10–40 °C), P/G/Si continued to display excellent shear thinning performance (Fig. 3I).

3.3. Characterization and properties of 3D-P/G/Si scaffolds

3.3.1. Characterization of 3D-P/G/Si scaffolds

The 3D-P/G/Si scaffolds were fabricated using extrusion printing technology, and their structural properties, such as the diameter of the printed filaments and the gap between the filaments, were finely adjusted by optimizing printing parameters including extrusion speed and printing pressure (Fig. 3J). In this study, we determined the optimal printing parameters for 18 G, 20 G, and 22 G printing nozzles respectively (Fig. 3K–N, Fig. S3, Supporting Information). To enhance accuracy in 3D printing, the 22G nozzle was employed in this study. As illustrated in Fig. S3, at a pressure of 2 bar, the filament diameter at the speed of 4 mm/s reached (784.75 ± 12.25) μm, while at the speed of 7 mm/s, it measured (402.43 ± 8.34) μm. These findings suggested that precise 3D printing can be achieved with a 22G nozzle by appropriately adjusting the printing pressure and speed. Subsequently, we evaluated the capability of P/G/Si printing ink to produce intricate 3D structures. Scaffolds with varying shapes, pore sizes, and thicknesses were printed using the 22G nozzle at a speed of 7 mm/s and a pressure of 2 bar. All scaffolds produced under these conditions demonstrated excellent stability without significant deformation, rendering them suitable for subsequent experiments(Fig. S4, Supporting Information). SEM further revealed that the surfaces of the 3D-P/G/Si scaffolds retained a rough and porous microstructure (Fig. 3O).

3.3.2. Mechanical properties

The mechanical properties and strength of the scaffolds were examined using tensile tests in this study (Fig. 4A, B). PVA exhibited the highest tensile strength (2680.06 ± 193.90) kPa, while P/G/Si hydrogel showed the lowest tensile strength (739.86 ± 48.89) kPa. The P/G hydrogel demonstrated a moderate strength of (1116.12 ± 144.16) kPa. Clearly, the addition of gelatin and nano-silica gradually decreased the tensile strength of the hydrogel, bringing its Young's modulus closer to that of native cartilage tissue (300–800 kPa) [45] (Fig. 4C,G). To further analyze the mechanical properties of the scaffolds, dumbbell specimens with pore sizes of 0, 400, and 800 μm were fabricated using 3D printing technology with P/G/Si printing ink for tensile testing purposes. Although different pore sizes resulted in variations among scaffolds under identical printing nozzles and parameters, all fell within the range of Young's modulus observed in cartilage tissue (Fig. 4D-F,H). This demonstrated our ability to customize auricular scaffolds by adjusting pore sizes in 3D printed scaffolds successfully. Furthermore, compared to printing ink prepared through traditional casting processes, the

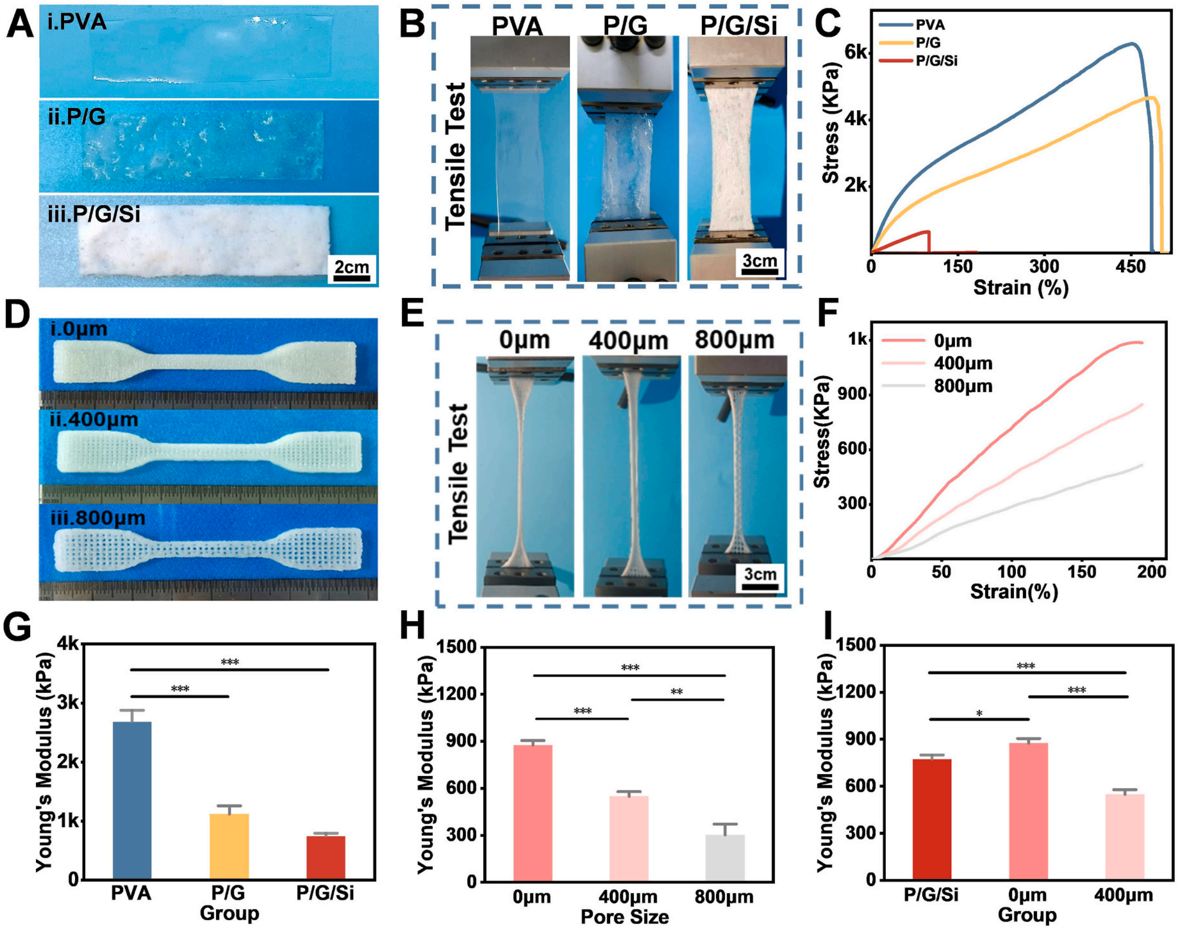

Fig. 4. Mechanical properties. (A) Mechanical test specimens of PVA, P/G, P/G/Si. (B) Tensile test of PVA, P/G, P/G/Si. (C) Tensile stress-strain curve of PVA, P/G, P/G/Si. (D) Mechanical test specimens of 3D-P/G/Si scaffolds with different pore sizes. (E) Tensile test of 3D-P/G/Si scaffolds with different pore sizes. (F) Tensile stress-strain curve of 3D-P/G/Si scaffolds with different pore sizes. (G–I) Young 's modulus (n = 3). Statistical analysis: *$P < 0.05$, **$P < 0.01$, ***$P < 0.001$.

3D-P/G/Si scaffold with a pore size of 0 μm displayed superior mechanical properties (Fig. 4I).

3.4. *Biocompatibility*

3.4.1. *In vitro*

The cytocompatibility and proliferative activity of C28/I2 cultured in scaffolds for 1 and 3 days are shown in Fig. 5A, where live cells are indicated by green fluorescence and dead cells by red fluorescence. After one day of culture, the cells adhered uniformly to the scaffold surface, with most cells in the PVA, P/G, and P/G/Si groups appearing green, indicating their viability. A small amount of red fluorescence was observed in the PVA group, while the number of red fluorescent cells was lower in the P/G group compared to the PVA group, suggesting better cell adhesion (Fig. 5Ai, ii). This discrepancy with the water contact angle results mentioned earlier was attributed to limited cell

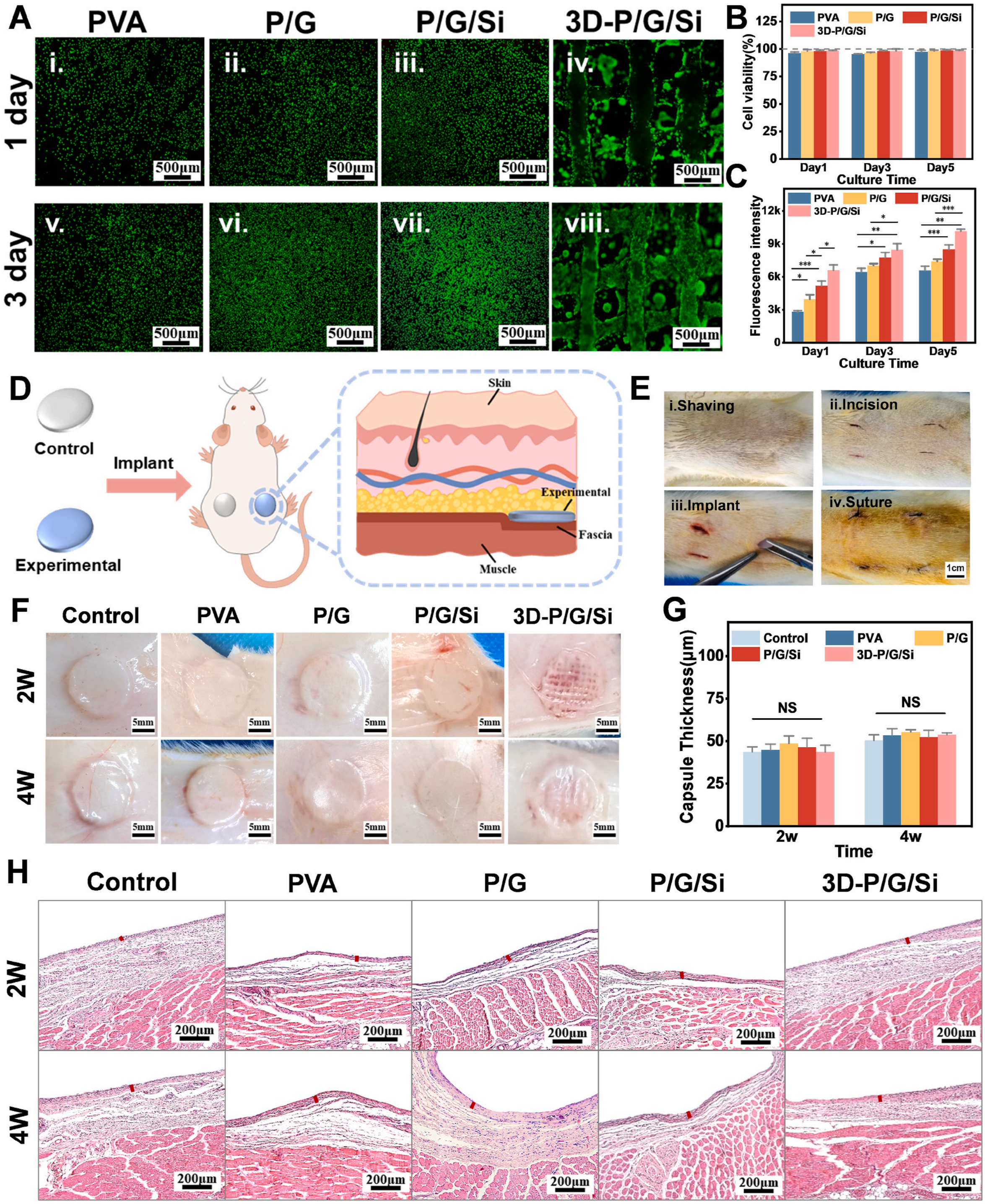

Fig. 5. Biocompatibility. (A) Live/Dead staining of C28/I2 cells. (B) Survival rate of C28/I2 cells (n = 3). (C) C28/I2 cells proliferation was measured by Alamar Blue assay (n = 3). (D) Schematic diagram of subcutaneous implantation in rats. (E) The process by which the sample is implanted under the skin of the rat's back. (F) Fiber wrapping around the sample at 2 and 4 weeks after implantation. (G) The thickness of fibrous capsule around the sample was measured at 2 and 4 weeks after implantation (n = 3). (H) H&E staining results of the tissue surrounding the sample at 2 and 4 weeks after implantation (red line: thickness of fibrous capsule). Statistical analysis: $^{*}P < 0.05$, $^{**}P < 0.01$, $^{***}P < 0.001$.

adhesion on the PVA surface. However, no red fluorescent cells were detected on samples from the P/G/Si group surface, indicating minimal cell death and significantly higher cell adhesion than both PVA and P/G groups (Fig. 5A iii). On day three of culture, Live/Dead staining revealed that most cells remained alive with a higher cell density than day one. The observed increase was particularly significant in the P/G/Si group (Fig. 5A v-vii).

To further evaluate cytocompatibility, C28/I2 cells were also seeded on 3D-P/G/Si scaffolds. Cell adhesion was not evident on day one of culture possibly due to the attachment of the cells was at an early stage and just attached to the pores of the scaffold (Fig. 5A iv). By day three though, there was a significant increase in C28/I2 cell adhesion on scaffold surfaces (Fig. 5A viii). Quantitative analysis demonstrated that after five days of culture, all experimental groups exhibited over 95 % survival rate for C28/I2 cells (Fig. 5B). Subsequently, the cell proliferation in each experimental group was assessed by measuring the fluorescence intensity change of Alamar Blue reagent. The results demonstrated that the fluorescence intensity of C28/I2 cells continued to increase after 1, 3, and 5 days, indicating normal growth and proliferation on different experimental group scaffolds with the 3D-P/G/Si scaffolds group exhibiting the highest proliferation rate (Fig. 5C).

3.4.2. *In vivo*

The scaffolds of each experimental group and control group were implanted subcutaneously in the back of SD rats, as illustrated in Fig. 5D. The entire process, including incision creation and specimen implantation suture, is depicted in Fig. 5E. Following implantation, the SD rats exhibited good overall health with normal eating and movement patterns. Skin tissue in contact with the specimens was collected after 2 and 4 weeks to evaluate fibrous capsule formation. As shown in Fig. 5F, no significant signs of inflammation or dense fibrous capsules were observed, indicating intact implants. Histological examination using H&E staining revealed comparable fibrous capsule thickness between the experimental and control groups across all examined skin tissues (Fig. 5G–H). Additionally, histological examination of vital organs (liver, heart, spleen, kidney) was conducted to further assess the biocompatibility of the experimental group. No significant inflammatory response or organ damage was observed in any group when compared to the control group. (Fig. 6, Fig. S5, Supporting Information).

3.5. *The immunofluorescence staining of type II collagen*

The C28/I2 cells were cultured with extracts of PVA, P/G, P/G/Si, and blank group. After 5 days, collagen II immunostaining was performed to observe the promoting effect of the hydrogel on chondrocytes. Simultaneously, DAPI was used for nuclear labeling of all cells. Quantitative analysis revealed that the positive fluorescence intensity of collagen II in the blank group was only (32.26 ± 3.48) %. In comparison, the PVA group and P/G group exhibited slightly higher levels, (40.84 ± 2 00.70) % and (37.78 ± 0.92) %, respectively. Notably, the P/G/Si group demonstrated significantly enhanced fluorescence intensity (48.26 ± 1.52) %, indicating a robust ability of the P/G/Si printing ink to promote chondrogenic differentiation (Fig. 7A–B).

3.6. *Animal auricular cartilage defect model*

To further verify the performance of the scaffold to promote cartilage formation, an investigation was conducted on rabbit auricular cartilage defect model. As illustrated in Fig. 7C, samples of both the experimental group and control group were implanted into the rabbit auricular cartilage defect model. Fig. 7D–F shows the whole process from the establishment of the cartilage defect model to the implantation of the experimental group and the control group, and compared the natural cartilage with all experimental materials. All rabbits were kept alive until the end of the experiment without complications. As shown in Fig. 7G–H, there was no evidence of infection or dehiscence at the surgical site, implant breakdown, or rejection of the implanted materials after 4 and 12 weeks. Cartilage regeneration was evaluated by histological morphological staining, including H&E, Alcian blue, Masson, SO/FG, Collagen I, and Collagen II. After 4 weeks post-operation, histological staining with H&E and Alcian blue revealed the presence of new chondrocytes at the fracture ends in the 3D-P/G/Si group, while chondrocyte proliferation was not evident in the other three groups

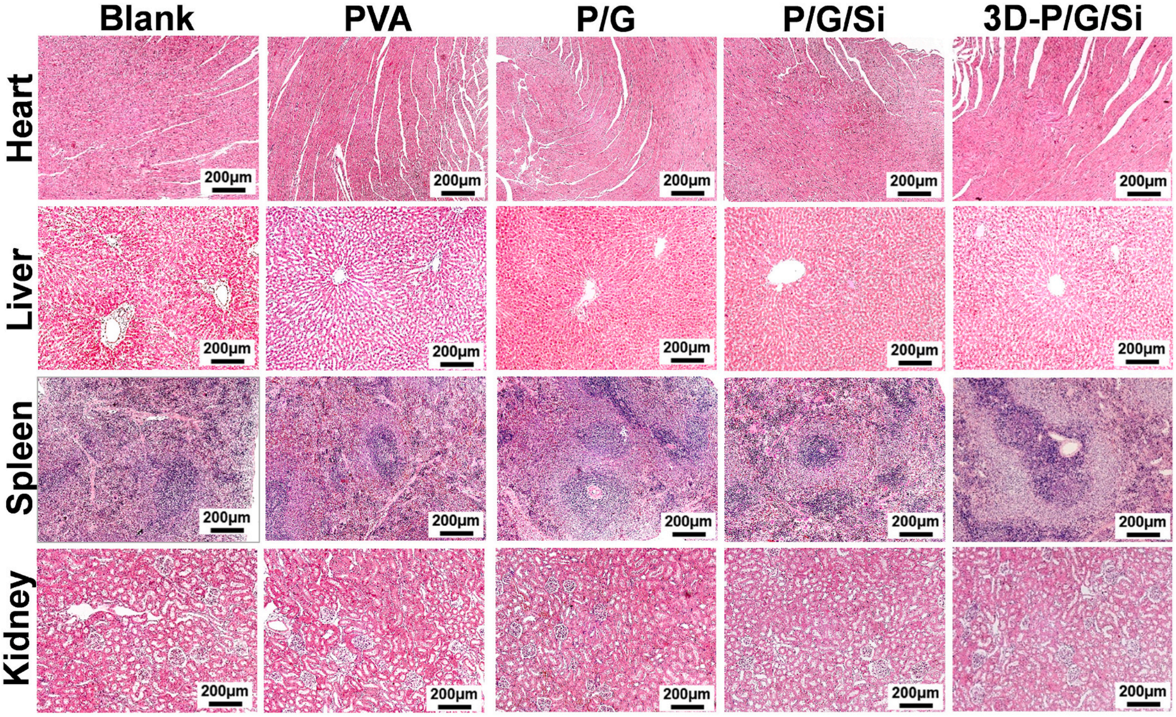

Fig. 6. H&E staining results of the heart, liver, spleen and kidney of rats 4 weeks after implantation.

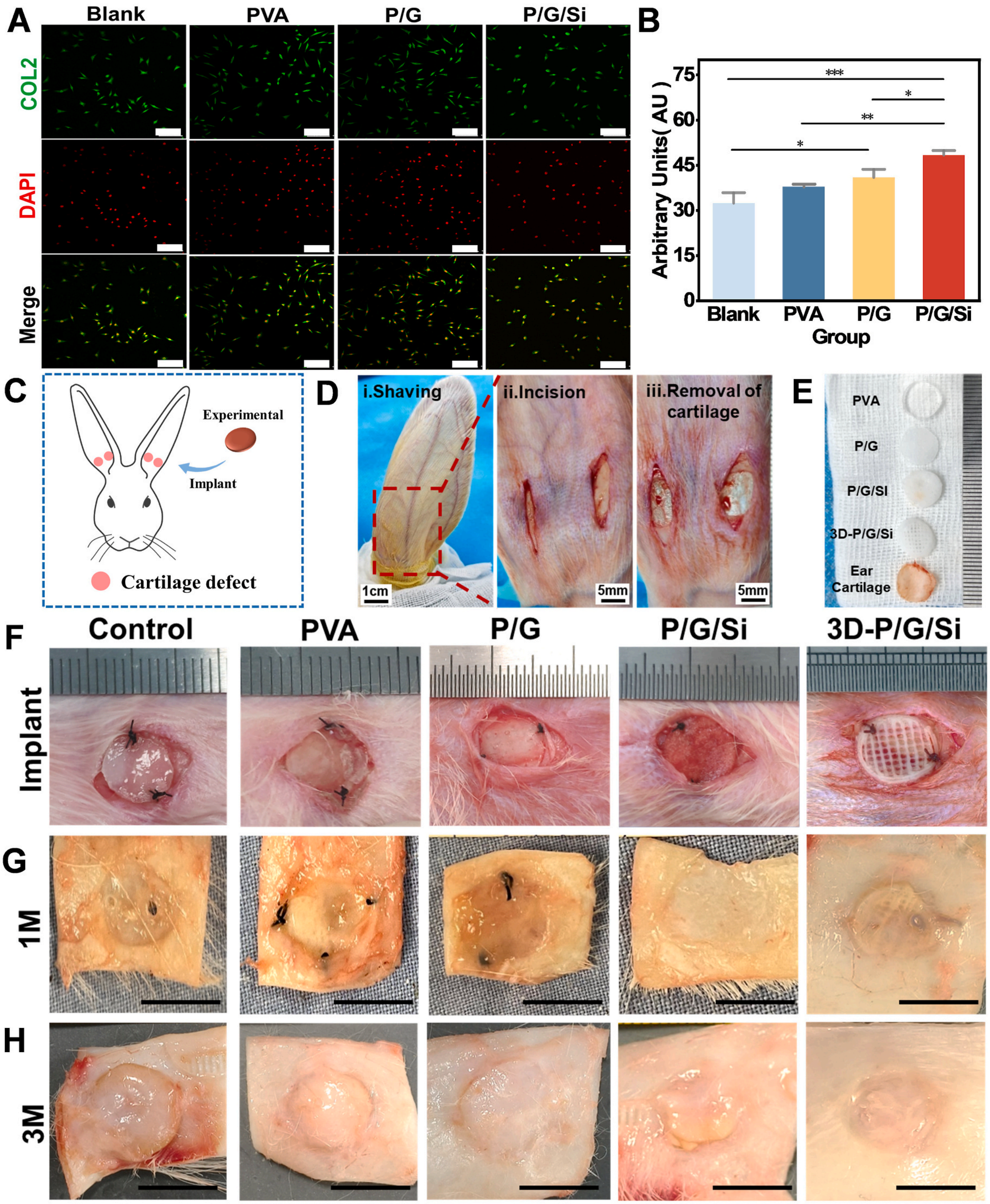

Fig. 7. Cartilage induction detection. (A) Collagen II/DAPI staining of C28/I2 cells. (B) Fluorescence intensity analysis of Collagen II (n = 3). (C) Schematic diagram of rabbit ear cartilage implantation. (D) Preparation process of rabbit ear cartilage defect model. (E) The PVA, P/G, P/G/Si, 3D-P/G/Si scaffolds were compared with rabbit auricular cartilage. (F) Implanted scaffolds. (G–H) Samples were taken at 1 and 3 months after implantation. Scale bars at panels A: 100 μm, G and H: 10 mm. Statistical analysis: $^*P < 0.05$, $^{**}P < 0.01$, $^{***}P < 0.001$.

(Fig. S6, Supporting Information). As depicted in Fig. 8 Ai-ii, fibrous tissue infiltration and limited cartilage repair capacity were observed at the defect site in both PVA and P/G groups after 12 weeks of surgery. Alcian blue staining also confirmed a small amount of chondrocyte proliferation within the defect area, with positive expression areas measuring only (5.84 ± 1.82) % for PVA group and (6.79 ± 0.95) % for P/G group. In the control group, a few long flat immature chondrocytes were observed at the edge of the defect area, exhibiting moderate intensity on Alcian blue staining with an expression area of (9.89 ± 0.82) %. Abundant new cartilage tissues characterized by increased cellularity and darker Alcian blue staining were observed in both P/G/Si and 3D-P/G/Si groups. The highest expression of Alcian blue was found in the 3D-P/G/Si group (14.21 ± 1.85) %, surpassing that seen in the P/G/Si group (11.75 ± 1.26) % (Fig. 8B). Similarly, immunohistochemical staining for Collagen I and Collagen II were also conducted in this study. The positive expression area of Collagen I was (37.62 ± 3.15) %, while the positive expression area of Collagen II was (33.93 ± 4.06) % in the 3D-P/G/Si group, both of which exhibited higher levels compared to

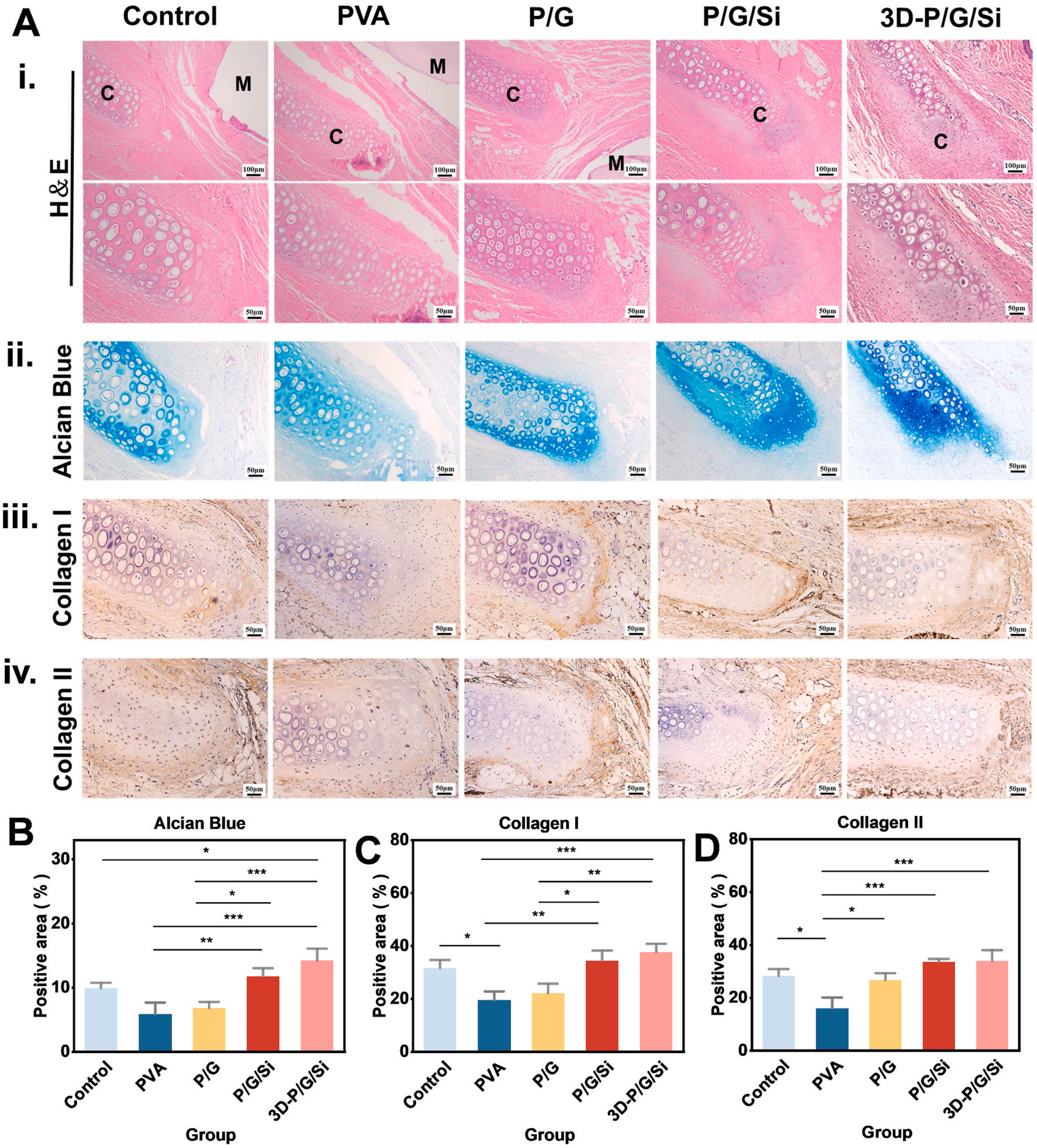

Fig. 8. Histological assessment of rabbit ear cartilage defect repair at 12 weeks. (A) H&E, Alcian Blue, Collagen I and Collagen II staining images of rabbit ear cartilage defect repair (C: rabbit ear cartilage, M: material for implantation). (B–D) Quantitation of immunohistochemical intensity of Alcian Blue, Collagen I and Collagen II (n = 3). Statistical analysis: *P < 0.05, **P < 0.01, ***P < 0.001.

other groups (Fig. 8A–D). Additionally, Masson staining and SO/FG staining demonstrated that the newly formed cartilage in the 3D-P/G/Si group exhibited strong staining. The cell morphology was largely preserved and arranged in an interwoven pattern, indicating a higher level of cartilage regeneration activity compared to the other experimental groups (Fig. S7, Supporting Information).

4. Discussion

To address the main clinical needs of auricular cartilage defects, a strategy based on biomaterials has recently been developed. This study provides a 3D printing P/G/Si scaffold forming method, which provides a new treatment idea for the personalized and precise treatment of microtia. Our results showed that (1) The P/G/Si hydrogel had excellent biocompatibility and the ability to promote cell proliferation. (2) The P/G/Si scaffold prepared using 3D printing technology met the high-precision anatomical requirements of human auricle and fitted the mechanical properties of auricular cartilage. (3) The 3D-P/G/Si scaffold created a repair environment for auricular cartilage regeneration and promoted cartilage growth (Fig. 1).

In this study, the results from ^{1}H NMR and ATR-IR analyses confirmed that successful cross-linking occurred as a result of the reaction between 6 M NaOH and specific functional groups in PVA. This reaction led to the breaking of hydrogen bonds and the deprotonation of the target groups. The newly formed O^- groups in PVA interacted with free Na^+ ions in solution, forming new complexes. Subsequently, immersion of the material in deionized water until pH = 7 facilitated removal of Na^+ ions, protonation of O^- groups, and permanent stabilization of crystalline domains, resulting in a robust, stretchable, and durable biomaterial (Fig. 2). However, the cell adhesion ability of PVA is limited, and it is difficult to form a good and stable relationship between cells and tissues [42]. The hydrophilicity of the material is related to the morphology of the material [46]. After adding Gel, the surface roughness decreased and the water contact angle in the fifth-second increased significantly. However, the addition of nano-silica increased the roughness of the hydrogel. Compared with the PVA and P/G groups, P/G/Si group showed a rougher and larger specific surface area under SEM. In addition, the appropriate swelling rate supports the absorption, moisture retention and nutrient exchange of the hydrogel in the wound [22]. In this study, the printing inks rapidly expanded in PBS and fully swelled within 24 h, and the swelling rate of P/G/Si group was three times that of PVA. The results of water contact angle and swelling showed that P/G/Si group had better hydrophilicity. Considering the longtime of cartilage regeneration, auricular reconstruction tissue engineering demands that the degradation rate of the scaffold should not be too rapid [47]. All groups of printing inks showed no significant degradation within 28 days, which could provide a stable environment for cartilage repair. The rheological properties of printing ink play a crucial role in determining the behavior of the entire 3D printing process [48]. Therefore, it is imperative to examine the rheological characteristics of printing ink, including their shear thinning behavior and viscoelasticity. P/G/Si retained its gel state as a viscoelastic solid over a temperature range of 10–40 °C. This characteristic facilitates retention of the filament shape after extrusion and enhances the fidelity of printed scaffold structures [43]. However, the behavior of PVA and P/G as fluids within this temperature range presented challenges in maintaining filament shape during 3D printing. Additionally, P/G/Si demonstrated excellent shear-thinning properties. In contrast, the low shear rate and inherent viscosity instability of PVA render it unsuitable for printing applications. In conclusion, we ultimately selected P/G/Si as our preferred printing ink for subsequent 3D printing and characterization performance testing.

Traditional casting fabrication makes it difficult to satisfy the high-precision anatomical structure of the auricle and cannot achieve personalized precision treatment [49]. 3D printing has the advantages of high processing flexibility and wide forming materials, which can meet the needs of complex structures and personalized manufacturing of auricle scaffold [50]. Therefore, in this study, a multi-layer porous auricular cartilage scaffold was prepared by 3D printing technology using P/G/Si as printing ink. Studies have shown that continuous and smooth filaments consistent with the inner diameter of the nozzle can only be obtained when the printing pressure and speed are properly matched [51]. By adjusting the pressure and speed, we obtained the optimal printing parameters of different sizes of nozzles (18G, 20G, 22 G). This proved that the printing ink can be adapted to different printing needs and purposes. To ensure the accuracy of printing, we finally chose the 22 G (400 μm) nozzle to continue the experiment. SEM showed that the 3D-P/G/Si scaffold had the advantages of high precision and a stable internal structure. 3D-P/G/Si still retained its surface roughness after printing (Fig. 3).

There have been many problems in the preparation of tissue engineering auricular scaffold materials. Among these, mechanical mechanics do not match the human auricular cartilage, resulting in collapse and shedding is a major problem [52,53]. The mechanical properties of PVA are different from those of human auricular cartilage, and can be improved by adding Gel and nano-silica. The mechanical strength of the P/G/Si hydrogel (739.86 ± 48.89 kPa) prepared in this study was within the range of natural cartilage tissue (300–800kpa) [45]. Therefore, the P/G/Si hydrogel with ideal mechanical properties can be used as auricular cartilage scaffold for tissue engineering. Furthermore, 3D printed scaffolds with different pore sizes were prepared, and it was found that the elastic modulus of the scaffolds could be adjusted by changing the pore size. The larger the pore size inside the scaffold, the lower the elastic modulus of the scaffold. Compared with P/G/Si hydrogel, the elastic modulus of the 3D printed scaffold with a pore size of 0 μm was higher, which may be due to the internal structure of the scaffold. Importantly, the mechanical strength of the 3D printed scaffold was within the range of natural cartilage tissue (Fig. 4).

In addition to the above characteristics, auricular reconstruction scaffold also requires good biocompatibility to promote cell adhesion, internal cartilage formation and new tissue regeneration [54]. Through experiments, we found that the three groups of printing inks had no cytotoxicity. The cell proliferation rate of P/G/Si group was higher than those of PVA group and P/G group. This can be attributed to the fact that with the addition of gelatin and nano-silica, the hydrogel can provide more adhesion anchor points for cells, making it easier for cells to adhere and proliferate in the hydrogel [55]. Compared to 2D structures, 3D printed scaffold provided a more physiological and organism-prone environment. Several studies have shown that an appropriate pore size is not only suitable for cell growth and adhesion but can also effectively promote chondrocyte differentiation [34]. We prepared a high-precision multi-layer 3D-P/G/Si scaffold with a pore size of 400 μm by printing technology. Compared with the P/G/Si hydrogel prepared by casting, the cells seeded on the scaffold proliferated faster. In the in vivo experiments, the experimental group materials were implanted subcutaneously in SD rats, and no obvious rejection was observed in the printing ink and 3D printed scaffolds (Figs. 5 and 6).

The type of collagen found in cartilage is mainly type II collagen. Collagen II is not only the main specific component of cartilage extracellular matrix but also a typical marker of mature chondrocyte differentiation [56,57]. In this study, general immunofluorescence staining confirmed that P/G/Si printing ink promoted the formation of Collagen II. To further evaluate the effect of scaffolds on cartilage regeneration in vivo, rabbit auricular cartilage defect model was established, and the scaffolds were implanted respectively. The newborn cartilage cells are long and flat, secreting proteoglycan, which can be confirmed by Alcian blue staining [58]. Furthermore, Masson staining, SO/FG staining, and immunohistochemical staining for Collagen I and Collagen II were employed to assess cartilage regeneration. The results of histological staining at 4 and 12 weeks after implantation showed that cartilage regeneration in the 3D-P/G/Si scaffold group was significantly higher than in the other groups. Combined with the results of in vitro and in vivo experiments, we propose that the scaffold has the potential to promote cartilage repair (Figs. 7 and 8). However, the present study has several limitations. First, the exact molecular mechanism by which P/G/Si printing ink promoted chondrogenesis has not been elucidated. Second, this study did not print a high-precision human auricular model based on the shape and structure of human natural auricular cartilage. Furthermore, to enhance the rigor of the existing in vivo cartilage repair experiments, it is essential to establish blank groups.

5. Conclusion

The printed multi-scale porous biomimetic scaffold with chondrogenic active ink was successfully fabricated to achieve a precise fit between the scaffold and human auricular cartilage. This multi-scale porous scaffold exhibits enhanced biological activity, conforms to the mechanical properties of human auricular cartilage, and is suitable for promoting chondrocyte growth. In this study, the efficacy of the bionic scaffold with a multi-scale and porous structure in treating auricular deformities was validated using a rabbit auricular cartilage defect model. It demonstrated that the bionic scaffold can create an optimal environment for auricular cartilage regeneration, offering novel insights into personalized and precise treatment approaches for auricular deformities.

CRediT authorship contribution statement

Yueying Kong: Writing – original draft, Methodology, Formal analysis, Data curation. **Zijing Lu:** Validation, Investigation, Conceptualization. **Jianan Zhan:** Methodology, Formal analysis. **Xi Zhou:** Validation, Investigation. **Shenghua Chen:** Formal analysis. **Qiwei Chen:** Software. **Haihuan Gong:** Software. **Xianlin Zhang:** Visualization. **Xiaoyan Mao:** Resources, Conceptualization. **Yilin Wang:** Writing – review & editing, Validation, Supervision, Conceptualization. **Wenhua Huang:** Resources, Project administration, Funding acquisition.

Declaration of competing interest

The authors declare that they have no known competing financial interests or personal relationships that could have appeared to influence the work reported in this paper.

Acknowledgments

Yueying Kong. and Zijing Lu contributed equally to this work. This work was financially supported by the National Natural Science Foundation of China (Grant No. 32271181). The authors would like to acknowledge those who contributed to this article.

Appendix A. Supplementary data

Supplementary data to this article can be found online at https://doi.org/10.1016/j.mtbio.2025.101516.

Data availability

Data will be made available on request.

References

[1] S. Humphries, A. Joshi, W.R. Webb, R. Kanegaonkar, Auricular reconstruction: where are we now? A critical literature review, Eur. Arch. Oto-Rhino-Laryngol. : official journal of the European Federation of Oto-Rhino-Laryngological Societies (EUFOS) : affiliated with the German Society for Oto-Rhino-Laryngology - Head and Neck Surgery 279 (2) (2022) 541–556.

[2] S. Gao, T. Nie, Y. Lin, L. Jiang, L. Wang, J. Wu, Y. Jiao, 3D printing tissue-engineered scaffolds for auricular reconstruction, Materials today. Bio 27 (2024) 101141.

[3] Y. Huang, H. Zhao, Y. Wang, S. Bi, K. Zhou, H. Li, C. Zhou, Y. Wang, W. Wu, B. Peng, J. Tang, B. Pan, B. Wang, Z. Chen, Z. Li, Z. Zhang, The application and progress of tissue engineering and biomaterial scaffolds for total auricular reconstruction in microtia, Front. Bioeng. Biotechnol. 11 (2023) 1089031.

[4] N. Khan, D.P. Zaki, W.E. Brown, F.F. Halaseh, D. Willette, M. Ziegler, K. A. Athanasiou, A.D. Widgerow, Tissue engineering auricular cartilage: a review of auricular cartilage characteristics and current techniques for auricular reconstruction, J. Craniofac. Surg. (2024).

[5] S. Landau, A.A. Szklanny, M. Machour, B. Kaplan, Y. Shandalov, I. Redenski, M. Beckerman, O. Harari-Steinberg, J. Zavin, O. Karni-Katovitch, I. Goldfracht, I. Michael, S.D. Waldman, S.I. Duvdevani, S. Levenberg, Human-engineered auricular reconstruction (hEAR) by 3D-printed molding with human-derived auricular and costal chondrocytes and adipose-derived mesenchymal stem cells, Biofabrication 14 (1) (2021).

[6] C.L. Reighard, S.J. Hollister, D.A. Zopf, Auricular reconstruction from rib to 3D printing, Journal of 3D printing in medicine 2 (1) (2018) 35–41.

[7] L. Ajmal, S. Ajmal, M. Ajmal, G. Nawaz, Organ regeneration through stem cells and tissue engineering, Cureus 15 (1) (2023) e34336.

[8] Y.Y. Fu, C.L. Li, J.L. Zhang, T.Y. Zhang, Autologous cartilage microtia reconstruction: complications and risk factors, Int. J. Pediatr. Otorhinolaryngol. 116 (2019) 1–6.

[9] C.M. Chiesa-Estomba, R. Hernáez-Moya, C. Rodiño, A. Delgado, G. Fernández-Blanco, J. Aldazabal, J. Paredes, A. Izeta, A. Aiastui, Ex vivo maturation of 3D-printed, chondrocyte-laden, polycaprolactone-based scaffolds prior to transplantation improves engineered cartilage substitute properties and integration, Cartilage 13 (4) (2022) 105–118.

[10] M. Griffin, D. Kalaskar, P. Butler, Argon plasma modified nanocomposite polyurethane scaffolds provide an alternative strategy for cartilage tissue engineering, J. Nanobiotechnol. 17 (1) (2019) 51.

[11] H.Y. Kim, S.Y. Jung, S.J. Lee, H.J. Lee, M.D. Truong, H.S. Kim, Fabrication and characterization of 3D-printed elastic auricular scaffolds: a pilot study, Laryngoscope 129 (2) (2019) 351–357.

[12] R.D. Childs, H. Nakao, N. Isogai, A. Murthy, W.J. Landis, An analytical study of neocartilage from microtia and otoplasty surgical remnants: a possible application for BMP7 in microtia development and regeneration, PLoS One 15 (6) (2020) e0234650.

[13] J. Zhou, Q. Li, Z. Tian, Q. Yao, M. Zhang, Recent advances in 3D bioprinted cartilage-mimicking constructs for applications in tissue engineering, Materials today, Bio 23 (2023) 100870.

[14] C. Antich, J. de Vicente, G. Jiménez, C. Chocarro, E. Carrillo, E. Montañez, P. Gálvez-Martín, J.A. Marchal, Bio-inspired hydrogel composed of hyaluronic acid and alginate as a potential bioink for 3D bioprinting of articular cartilage engineering constructs, Acta Biomater. 106 (2020) 114–123.

[15] Y. Chen, J. Zhang, X. Liu, S. Wang, J. Tao, Y. Huang, W. Wu, Y. Li, K. Zhou, X. Wei, S. Chen, X. Li, X. Xu, L. Cardon, Z. Qian, M. Gou, Noninvasive in vivo 3D bioprinting, Sci. Adv. 6 (23) (2020) eaba7406.

[16] P. Tang, P. Song, Z. Peng, B. Zhang, X. Gui, Y. Wang, X. Liao, Z. Chen, Z. Zhang, Y. Fan, Z. Li, Y. Cen, C. Zhou, Chondrocyte-laden GelMA hydrogel combined with 3D printed PLA scaffolds for auricle regeneration, Materials science & engineering, C, Materials for biological applications 130 (2021) 112423.

[17] M.M. De Santis, H.N. Alsafadi, S. Tas, D.A. Bölükbas, S. Prithiviraj, I.A.N. Da Silva, M. Mittendorfer, C. Ota, J. Stegmayr, F. Daoud, M. Königshoff, K. Swärd, J. A. Wood, M. Tassieri, P.E. Bourgine, S. Lindstedt, S. Mohlin, D.E. Wagner, Extracellular-matrix-Reinforced bioinks for 3D bioprinting human tissue, Advanced materials (Deerfield Beach, Fla.) 33 (3) (2021) e2005476.

[18] W. Liang, W. He, R. Huang, Y. Tang, S. Li, B. Zheng, Y. Lin, Y. Lu, H. Wang, D. Wu, Peritoneum-Inspired janus porous hydrogel with anti-deformation, anti-adhesion, and pro-healing characteristics for abdominal wall defect treatment, Advanced materials (Deerfield Beach, Fla.) 34 (15) (2022) e2108992.

[19] J. Lu, J. Huang, J. Jin, C. Xie, B. Xue, J. Lai, B. Cheng, L. Li, Q. Jiang, The design and characterization of a strong bio-ink for meniscus regeneration, International journal of bioprinting 8 (4) (2022) 600.

[20] I.C. Wu, J.W. Liou, C.H. Yang, J.H. Chen, K.Y. Chen, C.H. Hung, Self-assembly of gelatin and collagen in the polyvinyl alcohol substrate and its influence on cell adhesion, proliferation, shape, spreading and differentiation, Front. Bioeng. Biotechnol. 11 (2023) 1193849.

[21] I. Zulkiflee, M.B. Fauzi, Gelatin-polyvinyl alcohol film for tissue engineering: a concise review, Biomedicines 9 (8) (2021).

[22] Y. Ma, Y. Wang, D. Chen, T. Su, Q. Chang, W. Huang, F. Lu, 3D bioprinting of a gradient stiffened gelatin-alginate hydrogel with adipose-derived stem cells for full-thickness skin regeneration, J. Mater. Chem. B 11 (13) (2023) 2989–3000.

[23] J. Yang, K. Yang, W. Man, J. Zheng, Z. Cao, C.Y. Yang, K. Kim, S. Yang, Z. Hou, G. Wang, X. Wang, 3D bio-printed living nerve-like fibers refine the ecological niche for long-distance spinal cord injury regeneration, Bioact. Mater. 25 (2023) 160–175.

[24] G. Haghiashtiani, K. Qiu, J.D. Zhingre Sanchez, Z.J. Fuenning, P. Nair, S. E. Ahlberg, P.A. Iaizzo, M.C. McAlpine, 3D printed patient-specific aortic root models with internal sensors for minimally invasive applications, Sci. Adv. 6 (35) (2020) eabb4641.

[25] A. Lee, A.R. Hudson, D.J. Shiwarski, J.W. Tashman, T.J. Hinton, S. Yerneni, J. M. Bliley, P.G. Campbell, A.W. Feinberg, 3D bioprinting of collagen to rebuild components of the human heart, Science 365 (6452) (2019) 482–487. New York, N.Y.

[26] L. Zhang, W. Lee, X. Li, Y. Jiang, N.X. Fang, G. Dai, Y. Liu, 3D direct printing of mechanical and biocompatible hydrogel meta-structures, Bioact. Mater. 10 (2022) 48–55.

[27] M. Xie, J. Su, S. Zhou, J. Li, K. Zhang, Application of hydrogels as three-dimensional bioprinting ink for tissue engineering, Gels (Basel, Switzerland) 9 (2) (2023).

[28] H. Liu, H. Zhang, W. Han, H. Lin, R. Li, J. Zhu, W. Huang, 3D printed flexible strain sensors: from printing to devices and signals, Advanced materials (Deerfield Beach, Fla.) 33 (8) (2021) e2004782.

[29] D. Chimene, R. Kaunas, A.K. Gaharwar, Hydrogel bioink reinforcement for additive manufacturing: a focused review of emerging strategies, Advanced materials (Deerfield Beach, Fla.) 32 (1) (2020) e1902026.

[30] S. Sakai, A. Yoshii, S. Sakurai, K. Horii, O. Nagasuna, Silk fibroin nanofibers: a promising ink additive for extrusion three-dimensional bioprinting, Materials today. Bio 8 (2020) 100078.

[31] W. Xu, B.Z. Molino, F. Cheng, P.J. Molino, Z. Yue, D. Su, X. Wang, S. Willför, C. Xu, G.G. Wallace, On low-concentration inks formulated by nanocellulose assisted with gelatin methacrylate (GelMA) for 3D printing toward wound healing application, ACS applied materials & interfaces 11 (9) (2019) 8838–8848.

[32] S.A. Wilson, L.M. Cross, C.W. Peak, A.K. Gaharwar, Shear-thinning and thermo-reversible nanoengineered inks for 3D bioprinting, ACS applied materials & interfaces 9 (50) (2017) 43449–43458.

[33] R. Urruela-Barrios, E. Ramírez-Cedillo, A. Díaz de León, A.J. Alvarez, W. Ortega-Lara, Alginate/gelatin hydrogels reinforced with TiO_2 and β-TCP fabricated by microextrusion-based printing for tissue regeneration, Polymers 11 (3) (2019).

[34] M. Nelson, S. Li, S.J. Page, X. Shi, P.D. Lee, M.M. Stevens, J.V. Hanna, J.R. Jones, 3D printed silica-gelatin hybrid scaffolds of specific channel sizes promote collagen Type II, Sox9 and Aggrecan production from chondrocytes, Materials science & engineering, C, Materials for biological applications 123 (2021) 111964.

[35] M. Parkes, F. Tallia, G.R. Young, P. Cann, J.R. Jones, J.R.T. Jeffers, Tribological evaluation of a novel hybrid for repair of articular cartilage defects, Materials science & engineering, C, Materials for biological applications 119 (2021) 111495.

[36] N.C. Paxton, J. Dinoro, J. Ren, M.T. Ross, R. Daley, R. Zhou, K. Bazaka, R. G. Thompson, Z. Yue, S. Beirne, D.G. Harkin, M.C. Allenby, C.S. Wong, G. G. Wallace, M.A. Woodruff, Additive manufacturing enables personalised porous high-density polyethylene surgical implant manufacturing with improved tissue and vascular ingrowth, Appl. Mater. Today 22 (2021) 100965.

[37] S.H. Min, J.H. Kim, M.I. Lee, H.H. Kwak, H.M. Woo, J.H. Shim, D.M. Choi, J.S. Lee, J.Y. Jeong, B.J. Kang, Evaluation of auricular cartilage reconstruction using a 3-

dimensional printed biodegradable scaffold and autogenous minced auricular cartilage, Ann. Plast. Surg. 85 (2) (2020) 185–193.

[38] X.X. Zhang, B.Y. Liao, Z.J. Guan, K. Thakur, M.R. Khan, R. Busquets, J.G. Zhang, Z. J. Wei, Interaction between gelatin and mulberry leaf polysaccharides in miscible system: physicochemical characteristics and rheological behavior, Foods 11 (11) (2022).

[39] S. Liu, Q. Hu, Z. Shen, S. Krishnan, H. Zhang, M. Ramalingam, 3D printing of self-standing and vascular supportive multimaterial hydrogel structures for organ engineering, Biotechnol. Bioeng. 119 (1) (2022) 118–133.

[40] N. Bhamare, K. Tardalkar, P. Parulekar, A. Khadilkar, M. Joshi, 3D printing of human ear pinna using cartilage specific ink, Biomedical materials (Bristol, England) 16 (5) (2021).

[41] C. Shuai, F. Yang, Y. Shuai, S. Peng, S. Chen, Y. Deng, P. Feng, Silicon dioxide nanoparticles decorated on graphene oxide nanosheets and their application in poly(l-lactic acid) scaffold, J. Adv. Res. 48 (2023) 175–190.

[42] M.A. Darabi, A. Khosrozadeh, Y. Wang, N. Ashammakhi, H. Alem, A. Erdem, Q. Chang, K. Xu, Y. Liu, G. Luo, A. Khademhosseini, M. Xing, An alkaline based method for generating crystalline, strong, and shape memory polyvinyl alcohol biomaterials, Adv. Sci. 7 (21) (2020) 1902740.

[43] Y. Zeng, C. Huang, D. Duan, A. Lou, Y. Guo, T. Xiao, J. Wei, S. Liu, Z. Wang, Q. Yang, L. Zhou, Z. Wu, L. Wang, Injectable temperature-sensitive hydrogel system incorporating deferoxamine-loaded microspheres promotes H-type blood vessel-related bone repair of a critical size femoral defect, Acta Biomater. 153 (2022) 108–123.

[44] H. Gong, Y. Zhao, Q. Chen, Y. Wang, H. Zhao, J. Zhong, Q. Lan, Y. Jiang, W. Huang, 3D bio-printing of photocrosslinked anatomically tooth-shaped scaffolds for alveolar ridge preservation after tooth extraction, J. Mater. Chem. B 10 (41) (2022) 8502–8513.

[45] Y. Qu, S. He, S. Luo, J. Zhao, R. Liang, C. Liao, L. Zheng, Photocrosslinkable, injectable locust bean gum hydrogel induces chondrogenic differentiation of stem cells for cartilage regeneration, Adv. Healthcare Mater. 12 (18) (2023) e2203079.

[46] D. Kosoff, J. Yu, V. Suresh, D.J. Beebe, J.M. Lang, Surface topography and hydrophilicity regulate macrophage phenotype in milled microfluidic systems, Lab Chip 18 (19) (2018) 3011–3017.

[47] Y. Liu, G. Dzidotor, T.T. Le, T. Vinikoor, K. Morgan, E.J. Curry, R. Das, A. McClinton, E. Eisenberg, L.N. Apuzzo, K.T.M. Tran, P. Prasad, T.J. Flanagan, S. W. Lee, H.M. Kan, M.T. Chorsi, K.W.H. Lo, C.T. Laurencin, T.D. Nguyen, Exercise-induced piezoelectric stimulation for cartilage regeneration in rabbits, Sci. Transl. Med. 14 (627) (2022) eabi7282.

[48] S. Tajik, C.N. Garcia, S. Gillooley, L. Tayebi, 3D printing of hybrid-hydrogel materials for tissue engineering: a critical review, Regenerative engineering and translational medicine 9 (1) (2023) 29–41.

[49] J. Yin, J. Zhong, J. Wang, Y. Wang, T. Li, L. Wang, Y. Yang, Z. Zhen, Y. Li, H. Zhang, S. Zhong, Y. Wu, W. Huang, 3D-printed high-density polyethylene scaffolds with bioactive and antibacterial layer-by-layer modification for auricle reconstruction, Materials today. Bio 16 (2022) 100361.

[50] G. Zhou, H. Jiang, Z. Yin, Y. Liu, Q. Zhang, C. Zhang, B. Pan, J. Zhou, X. Zhou, H. Sun, D. Li, A. He, Z. Zhang, W. Zhang, W. Liu, Y. Cao, In vitro regeneration of patient-specific ear-shaped cartilage and its first clinical application for auricular reconstruction, EBioMedicine 28 (2018) 287–302.

[51] Y. Wang, X. Zhou, J. Zhong, J. Zhan, Y. Kong, J. Yin, H. Gong, Q. Chen, S. Li, H. Zhao, Y. Wu, W.J.A.F.M. Huang, Personalized Piezoresistive Anti-Scar Orthosis with Precise Pressure Monitoring Function Based on Embedded 3D Printing, 2024.

[52] G. Liu, Q. Wang, Q. Yang, L. Zhang, W. Dong, Y. Liu, R. Guo, J. Han, Mechanical study of polyurethane elastomer and Medpor as the material of artificial auricular scaffold, Zhongguo xiu fu chong jian wai ke za zhi = Zhongguo xiufu chongjian waike zazhi = Chinese journal of reparative and reconstructive surgery 33 (4) (2019) 492–496.

[53] J. Zeng, L. Jia, D. Wang, Z. Chen, W. Liu, Q. Yang, X. Liu, H. Jiang, Bacterial nanocellulose-reinforced gelatin methacryloyl hydrogel enhances biomechanical property and glycosaminoglycan content of 3D-bioprinted cartilage, International journal of bioprinting 9 (1) (2023) 631.

[54] J.M. Lee, M.T. Sultan, S.H. Kim, V. Kumar, Y.K. Yeon, O.J. Lee, C.H. Park, Artificial auricular cartilage using silk fibroin and polyvinyl alcohol hydrogel, Int. J. Mol. Sci. 18 (8) (2017).

[55] L. Ouyang, J.P.K. Armstrong, Q. Chen, Y. Lin, M.M. Stevens, Void-free 3D bioprinting for in-situ endothelialization and microfluidic perfusion, Adv. Funct. Mater. 30 (26) (2020) 1909009.

[56] D.V. Krishna, M.R. Sankar, P. Sarma, E.L. Samundeshwari, Copper nanoparticles loaded gelatin/polyvinyl alcohol/guar gum-based 3D printable multimaterial hydrogel for tissue engineering applications, Int. J. Biol. Macromol. 276 (Pt 1) (2024) 133866.

[57] R. Xu, J. Wu, L. Zheng, M. Zhao, Undenatured type II collagen and its role in improving osteoarthritis, Ageing Res. Rev. 91 (2023) 102080.

[58] Y. Yu, L. Lin, K. Liu, Y. Jiang, Z. Zhou, Effects of simvastatin on cartilage homeostasis in steroid-induced osteonecrosis of femoral head by inhibiting glucocorticoid receptor, Cells 11 (24) (2022).